



Satellite solar-induced chlorophyll fluorescence and near-infrared reflectance capture complementary aspects of dryland vegetation productivity dynamics

Xian Wang^{a,*}, Joel A. Biederman^b, John F. Knowles^{b,c}, Russell L. Scott^b, Alexander J. Turner^d, Matthew P. Dannenberg^e, Philipp Köhler^f, Christian Frankenberg^f, Marcy E. Litvak^g, Gerald N. Flerchinger^h, Beverly E. Lawⁱ, Hyojung Kwonⁱ, Sasha C. Reed^j, William J. Parton^k, Greg A. Barron-Gafford^c, William K. Smith^{a,*}

^a School of Natural Resources and the Environment, University of Arizona, Tucson, AZ, USA

^b Southwest Watershed Research Center, USDA Agricultural Research Service, Tucson, AZ, USA

^c School of Geography, Development and Environment, University of Arizona, Tucson, AZ, USA

^d Department of Atmospheric Sciences, University of Washington, Seattle, WA, USA

^e Department of Geographical and Sustainability Sciences, University of Iowa, Iowa City, IA, USA

^f Division of Geological and Planetary Sciences, California Institute of Technology, Pasadena, CA, USA

^g Department of Biology, University of New Mexico, Albuquerque, NM, USA

^h Northwest Watershed Research Center, USDA Agricultural Research Service, Boise, ID, USA

ⁱ Department of Forest Ecosystems and Society, College of Forestry, Oregon State University, Corvallis, OR, USA

^j Southwest Biological Science Center, U.S. Geological Survey, Moab, UT, USA

^k Natural Resource Ecology Laboratory, Colorado State University, Fort Collins, CO, USA

ARTICLE INFO

Editor: Jing M. Chen

Keywords:

Gross primary productivity
Dryland heterogeneity
Remote sensing
Near-infrared reflectance
Solar-induced fluorescence

ABSTRACT

Mounting evidence indicates dryland ecosystems play an important role in driving the interannual variability and trend of the terrestrial carbon sink. Nevertheless, our understanding of the seasonal dynamics of dryland ecosystem carbon uptake through photosynthesis [gross primary productivity (GPP)] remains relatively limited due in part to the limited availability of long-term data and unique challenges associated with satellite remote sensing across dryland ecosystems. Here, we comprehensively evaluated longstanding and emerging satellite vegetation proxies in their ability to capture seasonal dryland GPP dynamics. Specifically, we evaluated: 1) reflectance-based proxies normalized difference vegetation index (NDVI), soil adjusted vegetation index (SAVI), near infrared reflectance index (NIR_v), and kernel NDVI (kNDVI) from the MODerate resolution Imaging Spectroradiometer (MODIS); and 2) newly available physiologically-based proxy solar-induced chlorophyll fluorescence (SIF) from the TROPOspheric Monitoring Instrument (TROPOMI). As a performance benchmark, we used GPP estimates from a robust network of 21 western United States eddy covariance tower sites that span representative gradients in dryland ecosystem climate and functional composition. We found that NIR_v and SIF were the best performing GPP proxies and captured complementary aspects of seasonal GPP dynamics across dryland ecosystem types. NIR_v offered better performance than the other proxies across relatively low-productivity, sparsely non-evergreen vegetated sites ($R^2 = 0.59 \pm 0.13$); whereas SIF best captured seasonal dynamics across relatively high-productivity sites, including evergreen-dominated sites ($R^2 = 0.74 \pm 0.07$). Notably, across grass-dominated sites, all reflectance-based proxies (NDVI, SAVI, NIR_v and kNDVI) showed significant seasonal bias (hysteresis) that strengthened with the total fraction of woody vegetation cover, likely due to seasonal patterns in woody vegetation reflectance that are unrelated to or decoupled from GPP. Future efforts to fully integrate the complementary strengths of NIR_v and SIF could significantly improve our understanding and representation of dryland GPP dynamics in satellite-based models.

* Corresponding authors.

E-mail addresses: xianwang@email.arizona.edu (X. Wang), wksmith@email.arizona.edu (W.K. Smith).

<https://doi.org/10.1016/j.rse.2021.112858>

Received 28 February 2021; Received in revised form 7 December 2021; Accepted 18 December 2021

Available online 31 December 2021

0034-4257/© 2021 Elsevier Inc. All rights reserved.

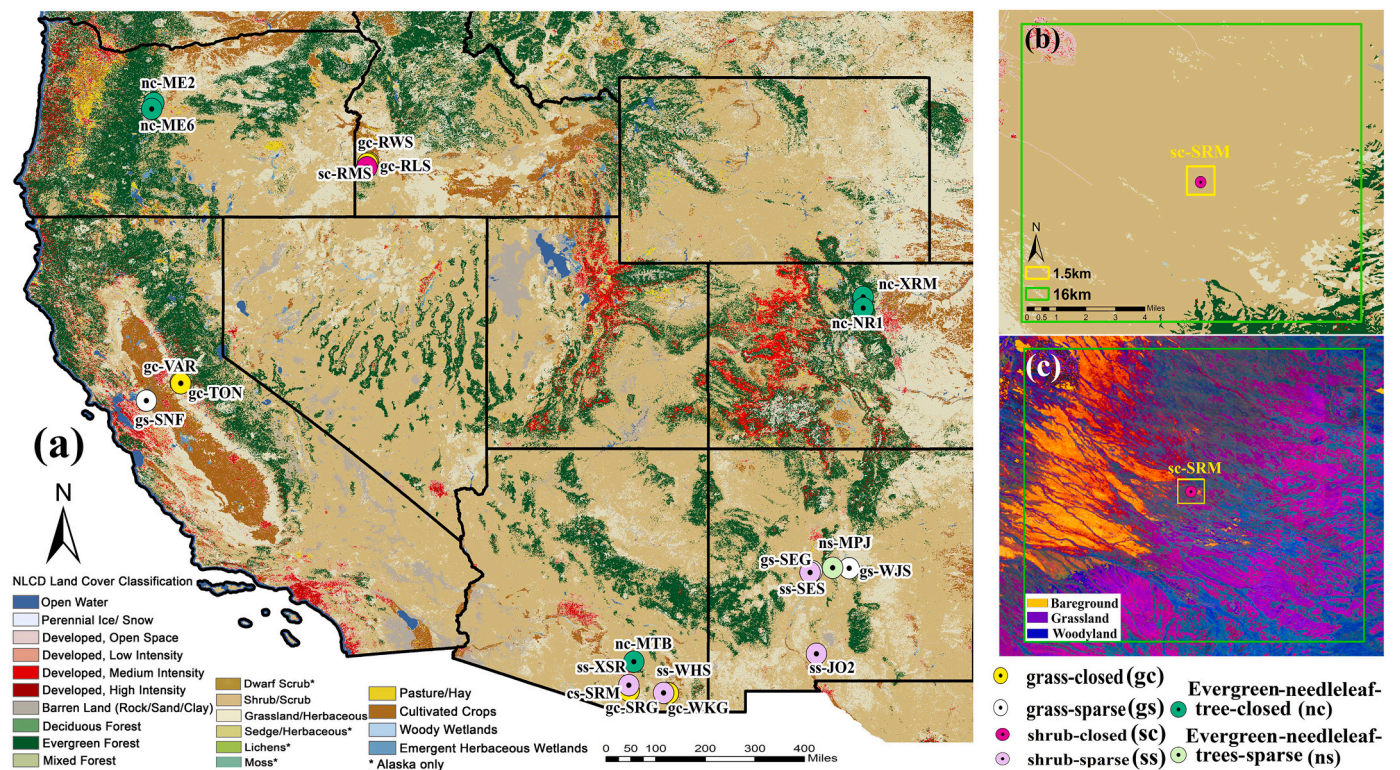


Fig. 1. (a) Locations of the 21 eddy covariance tower (EC) sites distributed across the western US. Abbreviations correspond to the AmeriFlux network site codes and symbol colors denote prevailing ecosystem type. Base map shows the 2016 Landsat-based National Land Cover Database (NLCD). (b) The sc-SRM EC site with 1.5-km² and 16-km² buffers against the 2016 NLCD data product background. (c) The sc-SRM EC site with 1.5-km² and 16-km² buffers against an RGB composite background showing the three major vegetation covers: 11% bare ground, 28% grass, and 29% woody (shrub+tree) within a 1.5-km² grid and 14% bare ground, 26% grass, and 30% woody covers within a 16-km² grid.

1. Introduction

Dryland ecosystems cover more than 40% of Earth's land surface and are a major driver of the interannual variability and subsequent trend in the terrestrial carbon sink (Poulter et al., 2014; Ahlstrom et al., 2015; Smith et al., 2019). A better understanding of these critical ecosystems is urgently needed, since aridity is projected to increase with climate change, potentially resulting in the expansion of drylands to more than half of the planet's terrestrial surface by 2100 (Reynolds et al., 2007; Huang et al., 2016, 2017; Yao et al., 2020). Yet, despite their emerging importance, there remains limited availability of continuous, long-term measurements of carbon cycling in dryland regions, resulting in data products that are poorly constrained (Biederman et al., 2017).

Satellite observations have provided key insights into dryland GPP dynamics over the last four decades (Smith et al., 2019), and have been used as observational input in numerous satellite-based GPP products (Smith et al., 2016; Bodesheim et al., 2018; Robinson et al., 2018). Yet, GPP cannot be directly observed and satellite-based GPP products have been found to perform relatively poorly across heterogeneous dryland regions (Verma et al., 2014; Biederman et al., 2017). For example, the widely-used MODerate resolution Imaging Spectroradiometer (MODIS) GPP product captured only about 30% of the interannual variation in GPP observations across a network of dryland eddy covariance tower (EC) sites in United States (US) (Biederman et al., 2017). This is due in large part to unique challenges associated with drylands, which represent dynamic mixtures of herbaceous, woody, and bare soil components, that limit the ability of common satellite vegetation proxies, such as the normalized difference vegetation index (NDVI), in their ability to track vegetation function (Smith et al., 2018; Allred et al., 2020; Ma et al., 2020).

Multiple surface reflectance-based proxies have been developed to

better constrain our understanding of dryland GPP including soil adjusted vegetation index (SAVI), near infrared reflectance index (NIR_v), and kernel NDVI (kNDVI). SAVI and NIR_v are thought to reduce the confounding effects of background soil brightness (Huete, 1988; Badgley et al., 2017), and NIR_v is also thought to capture the depth distribution of canopy photosynthetic capacity, thus more accurately capturing changes in structurally complex landscapes (Badgley et al., 2017, 2019; Baldocchi et al., 2020). The recently developed kNDVI was designed to exploit all higher-order relationships between the input surface reflectance observations, and thus better represent any non-linearity in the NDVI:GPP relationship (Camps-Valls et al., 2021). Yet, to our knowledge, these reflectance-based proxies, particularly NIR_v and kNDVI, have not been comprehensively evaluated across dryland ecosystem types specifically.

Solar-induced chlorophyll fluorescence (SIF) is a promising advance in remote sensing and fundamentally different from the above vegetation reflectance-based proxies. SIF is not based on vegetation reflectance, but instead a measure of radiance emitted by the vegetation during the light reactions of photosynthesis. SIF is unique in that it has both physical and physiological controls, and thus may represent a critical advance in our ability to track GPP (Joiner et al., 2014; Walther et al., 2016). Previous studies have indicated a near-linear relationship with GPP, but the extent to which factors such as environmental condition and spatial heterogeneity mediate the SIF:GPP relationship remains unresolved and an area of active research (Guanter et al., 2007, 2014; Sun et al., 2017; Smith et al., 2018). A particular advantage of SIF is its apparent ability to track changes in GPP even in the absence of changes in spectral reflectance (Smith et al., 2018; Zuromski et al., 2018; Magney et al., 2019). Surface reflectance-based proxies often overestimate GPP when plants are green but photosynthetically inactive (e.g., evergreen species during periods of severe drought), which can result

in seasonal hysteretic relationships between these proxies and GPP (Gitelson et al., 2014; Flanagan et al., 2015; Nestola et al., 2016; Wang et al., 2020a). The recently launched TROPospheric Monitoring Instrument (TROPOMI) represents a revolutionary advance in SIF observation by providing daily global coverage and relatively high spatial resolution (Köhler et al., 2018). With TROPOMI SIF estimates, we have a first-time opportunity to fully evaluate at relatively high spatiotemporal resolution the potential of SIF for improving seasonal GPP estimates across dryland ecosystems.

Drylands have long been recognized as useful test-beds for evaluating satellite proxies in their ability to track different aspects of vegetation dynamics (Tucker, 1979; Smith et al., 2019). However, it remains unclear how factors like functional and structural diversity, such as bare ground exposure, impact these evaluations (Smith et al., 2019). Dryland vegetation communities are characterized by a seasonally dynamic mixture of annual and perennial grasses, shrubs and trees growing individually or in small groups, and exposed bare ground (Brandt et al., 2020). Yet, these heterogeneous mixtures of functional types are classified as simply grass- or shrub-dominated in widely used land cover classifications including the National Land Cover Database (NLCD) (Dewitz, 2019). As a result, the importance of functional and structural diversity in influencing the relationship between satellite proxies and ecosystem function has been underexplored (Smith et al., 2019). The availability of new fractional vegetation cover products that quantify heterogeneity in annual and perennial grasses, shrubs, trees, and bare ground at the sub-pixel level provide a first opportunity to address this knowledge gap and quantify the mediating role of functional and structural diversity in influencing the relationship between the above identified satellite proxies and ecosystem GPP (Jones et al., 2018; Allred et al., 2020).

Here, we comprehensively evaluate NDVI, kNDVI, NIR_v, SAVI, and SIF in their ability to capture seasonal dryland GPP dynamics. As a performance benchmark, we used GPP estimates from a robust network of 21 western US eddy covariance tower sites that span representative gradients in dryland ecosystem climate and functional composition. We further integrate a new fractional vegetation cover product, the Rangeland Analysis Product (Allred et al., 2020), to fully classify each site by its functional type heterogeneity. Our over-arching research questions are: (1) how well do reflectance-based proxies (NDVI, SAVI, NIR_v, and kNDVI) and a physiologically-based proxy (SIF) track seasonal GPP dynamics across dryland ecosystems? (2) how does functional heterogeneity of dryland ecosystems mediate the performance of these two distinct classes of vegetation GPP proxies? (3) can a simply integrated proxy perform best by combining the independent strengths of reflectance-based and physiologically-based proxies?

2. Methods

2.1. Study area and land cover classification

We used GPP estimates from 21 EC sites distributed across ecological sub-regions of the western US (Fig. 1, Table S1) (Biederman et al., 2017; Smith et al., 2018). Daily GPP was averaged from half-hour observations of GPP at each EC site between April 2018 and December 2019 (Fig. 1, Table S1; ameriflux.lbl.gov). The widely used partitioning algorithm (Reichstein et al., 2005; Lasslop et al., 2010) was used to partition the net ecosystem exchange of CO₂ flux into GPP and ecosystem respiration.

EC sites were classified as shrub-sparse, shrub-closed, grass-sparse, grass-closed, evergreen-needleleaf-tree-sparse, and evergreen-needleleaf-tree-closed using 30-m fractional land cover estimates for the year 2019 from the Rangeland Cover V2.0 data product (Allred et al., 2020) (Fig. 1, Table S1). We first calculated the mean fractional cover of bare ground, grass, shrub, and tree within a 1.5-km² and 16-km² area around each EC site. We note that sites may have some photosynthetic soil cover (i.e., biological soil crusts; Ferrenberg et al., 2017), and this cover was categorized as bare ground. While incorporating biological

soil crust cover may help improve dryland GPP assessments in the future (Smith et al., 2019), those data do not currently exist and are beyond the scope of this study.

Sites with tree cover as the largest fractional cover within 1.5-km² of the EC tower were classified as tree-dominant sites. We used the ratio between woody (tree+shrub) and total vegetation coverage (Ratio1) to define shrub-dominant and grass-dominant sites. Sites that were not tree-dominated and Ratio1 > 0.4 were classified as shrub-dominated; otherwise, sites that were not tree-dominated and with Ratio1 ≤ 0.4 were classified as grass-dominated. We then used the ratio between bare ground and vegetation (Ratio2) to define the vegetation openness. If Ratio2 > 0.2, the site was considered densely vegetated (“-closed”); otherwise the site was considered to be sparsely vegetated (“-sparse”). The sparse site with mean GPP < 1 μmol CO₂ m⁻² s⁻¹ in the period of April 2018 to December 2019 was further considered as low-productivity, otherwise, the site was considered as high-productivity. In total, this resulted in 9 grass and 6 shrub sites with 8 closed and 7 sparse, as well as 7 low-productivity and 8 high-productivity for a well-balanced classification of the available sites (Fig. 1, Table S2). Based on the above criteria, we classified EC sites RWS, WKG, SRG, TON, VAR, and RLS as grass-closed (gc); SEG, SNF, and WJS as grass-sparse (gs); RMS and SRM as shrub-closed (sc); SES, JO2, XSR, and WHS as shrub-sparse (ss); ME2, MTB, ME6, XRM, and NR1 as evergreen-needleleaf-tree-closed (nc); as well as MPJ as evergreen-needleleaf-tree-sparse (ns) (Fig. 1, Table S2). Hereafter, we also included the prefix of the vegetation classification abbreviations in the site name to be more informative. We note that nc-ME6 and gs-WJS are not typically classified as closed and grass-sparse ecosystems, respectively (Law and Waring, 2011), which could result either from our classification method or classification errors in the Rangeland Cover V2.0 product. In addition, the Rangeland cover product does not include evergreen vegetation cover, which we instead obtained from the 2016 NLCD product (<https://www.mrlc.gov/data/nlcd-2016-land-cover-conus>).

2.2. MODIS vegetation reflectance-based proxies

We calculated the NDVI, kNDVI, NIR_v, and SAVI from daily 500-m resolution nadir BRDF-adjusted reflectance (MCD43A4) data, which we refer to reflectance-based proxies in this study. The data quality was controlled by removing all pixels that were not classified as either “good” (QA = 0) or “marginal” (QA = 1) quality in the QA layer. NDVI is defined as the normalized difference between near-infrared (NIR: MCD43A4 Band 2) and red (Red: MCD43A4 Band 1) reflectance (Sellers et al., 1992):

$$NDVI = \frac{(NIR - Red)}{(NIR + Red)} \quad (1)$$

kNDVI is a nonlinear generalization of NDVI (Camps-Valls et al., 2021):

$$kNDVI = \tanh \left(\left(\frac{NIR - Red}{2\sigma} \right)^2 \right) \quad (2)$$

where σ is a tunable length-scale parameter intended to capture non-linear sensitivity of NDVI to vegetation density. Following Camps-Valls et al. (2021), we use the generalization $\sigma = 0.5(NIR + red)$, which simplifies Eq. (2) to $kNDVI = \tanh((NDVI)^2)$.

NIR_v is designed to better represent the depth-distribution of canopy photosynthetic capacity and is calculated as the product of the NDVI and NIR bands (Badgley et al., 2017):

$$NIR_v = (NDVI - 0.08) \times NIR \quad (3)$$

SAVI accounts for differential red and near-infrared extinction through the vegetation canopy and utilizes a transformation technique to minimize soil brightness influences (Huete, 1988):

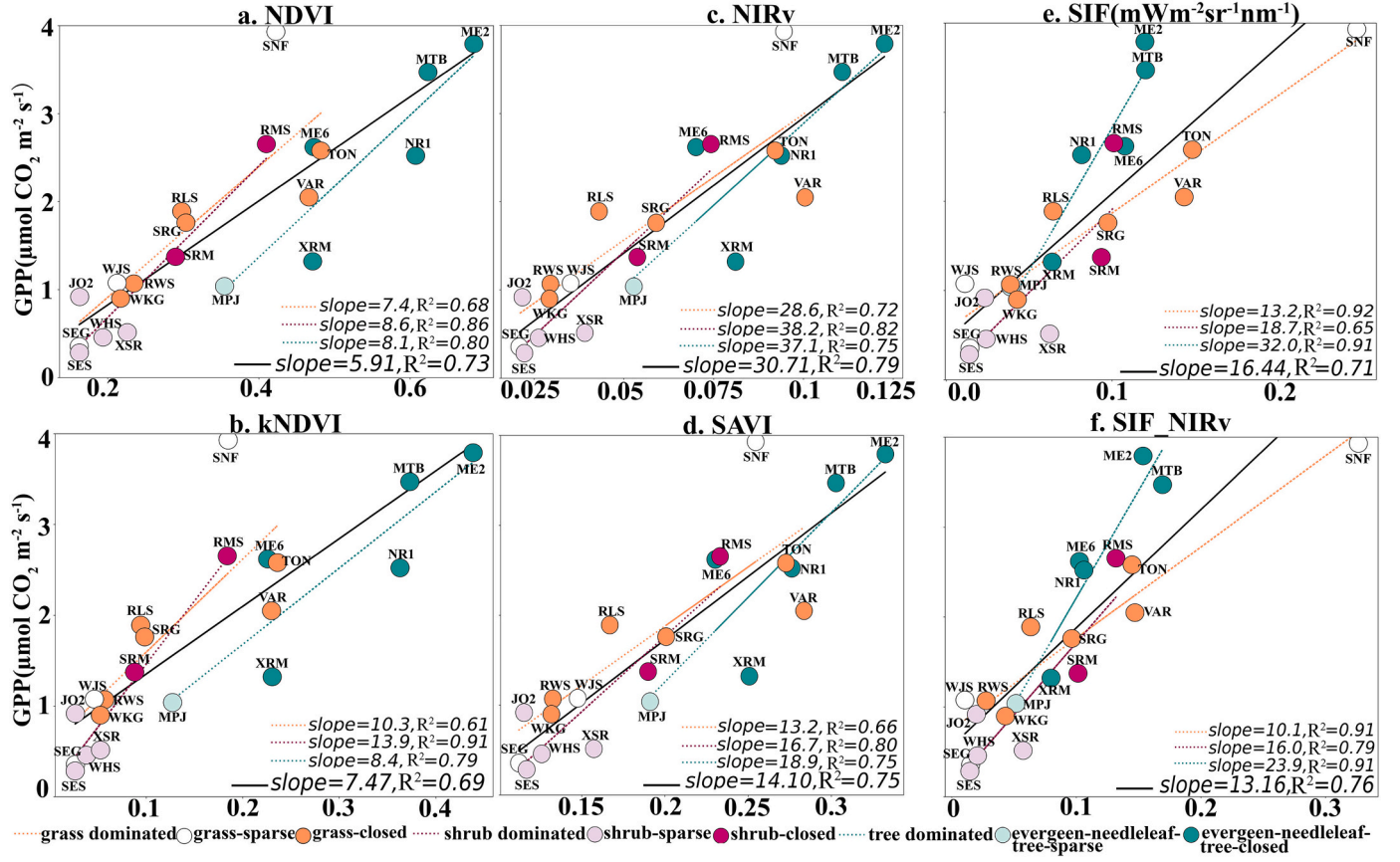


Fig. 2. A comparison of mean EC GPP and (a) mean NDVI (1.5-km²), (b) mean kNDVI (1.5-km²), (c) mean NIR_v (1.5-km²), (d) mean SAVI (1.5-km²), (e) mean SIF (16-km²), and (f) mean SIF downscaled by NIR_v (SIF_NIR_v; 1.5-km²) over the study period from April 2018 to December 2019 across shrub-dominated, grass-dominated, and evergreen-needleleaf- tree-dominated sites.

$$SAVI = \frac{(1 + L) \times (NIR - Red)}{(NIR + Red + L)} \quad (4)$$

where L is a soil brightness correction factor. The value of L varies with the amount or cover of green vegetation: in very high vegetation regions, $L = 0$, and in areas with no green vegetation, $L = 1$. Here, we used $L = 0.5$ (the default value), which works well in most situations (Richardson and Everitt, 1992).

2.3. TROPOMI SIF data

We obtained daily TROPOMI SIF data between April 2018 and December 2019 from <http://fluio.gps.caltech.edu/data/tropomi/ungridded/>. TROPOMI ground pixels are 5.6-km along-track and vary from 3.5–14 km across-track (nadir to 60° viewing angle). The data were pre-processed using a data-driven approach to separate SIF emissions from the reflected solar radiation. The data were subsequently restricted to 20–200 mW m⁻²sr⁻¹nm⁻¹ and filtered for pixels with visible infrared imaging radiometer suite cloud fractions larger than 0.8 and view zenith angles (VZAs) lower than 60 degrees. We converted instantaneous SIF observations to integrated daily SIF estimates by multiplying instantaneous SIF by the daily correction factor that was made available with the data product (Köhler et al., 2018; Doughty et al., 2019). We averaged all available SIF retrievals within a 16-km² grid centered on each EC site (Fig. 1).

2.4. SIF downscaling

While the spatial resolution of TROPOMI SIF (5.6-km × 3.5-km at nadir) is relatively fine compared to retrievals from previous sensors (e.

g. GOME-2), there remains a considerable spatial mismatch between TROPOMI and the average footprint of EC sites (Turner et al., 2020; Chu et al., 2021). To enhance the spatial resolution of TROPOMI SIF observations, Turner et al. (2020) developed a spatial downscaling approach that statistically integrated TROPOMI SIF and MODIS NIR_v observations to generate a 500-m SIF product (SIF_NIR_v). SIF_NIR_v was demonstrated to be an effective GPP proxy capable of accurately detecting interannual GPP variability across the conterminous US (Turner et al., 2020, 2021). We therefore also combined the SIF and NIR_v signals into a downscaled SIF product at 500 m resolution that we refer as SIF_NIR_v (Turner et al., 2020):

$$(SIF_NIR_v)_{ij} = SIF \times \left((NIR_v)_{ij} \div NIR_v \right) \quad (5)$$

where i and j indicate the row and column number of each pixel in the 16-km² grid, $(SIF_NIR_v)_{ij}$ and $(NIR_v)_{ij}$ are SIF_NIR_v and NIR_v for each MODIS cell, and SIF and NIR_v are means of $(SIF_NIR_v)_{ij}$ and $(NIR_v)_{ij}$ within the 16 km² footprint. For each EC tower, $(SIF_NIR_v)_{ij}$ was calculated for each MODIS cell within the 16-km² grid, then the mean SIF_NIR_v was calculated as the average $(SIF_NIR_v)_{ij}$ within a 1.5-km² area centered on the flux tower, in order to most accurately match the tower flux footprint (Fig. S1; Chu et al., 2021).

2.5. Comparison of satellite-based proxies with eddy covariance GPP

We calculated the daily averages of NDVI, kNDVI, NIR_v, SAVI and SIF_NIR_v in a 1.5-km² area centered on each EC site, and TROPOMI SIF across the corresponding 16-km² grid. Within the larger grid, we only retained TROPOMI SIF retrievals with the same vegetation cover as the target EC site. Averages of all vegetation covers were calculated in the

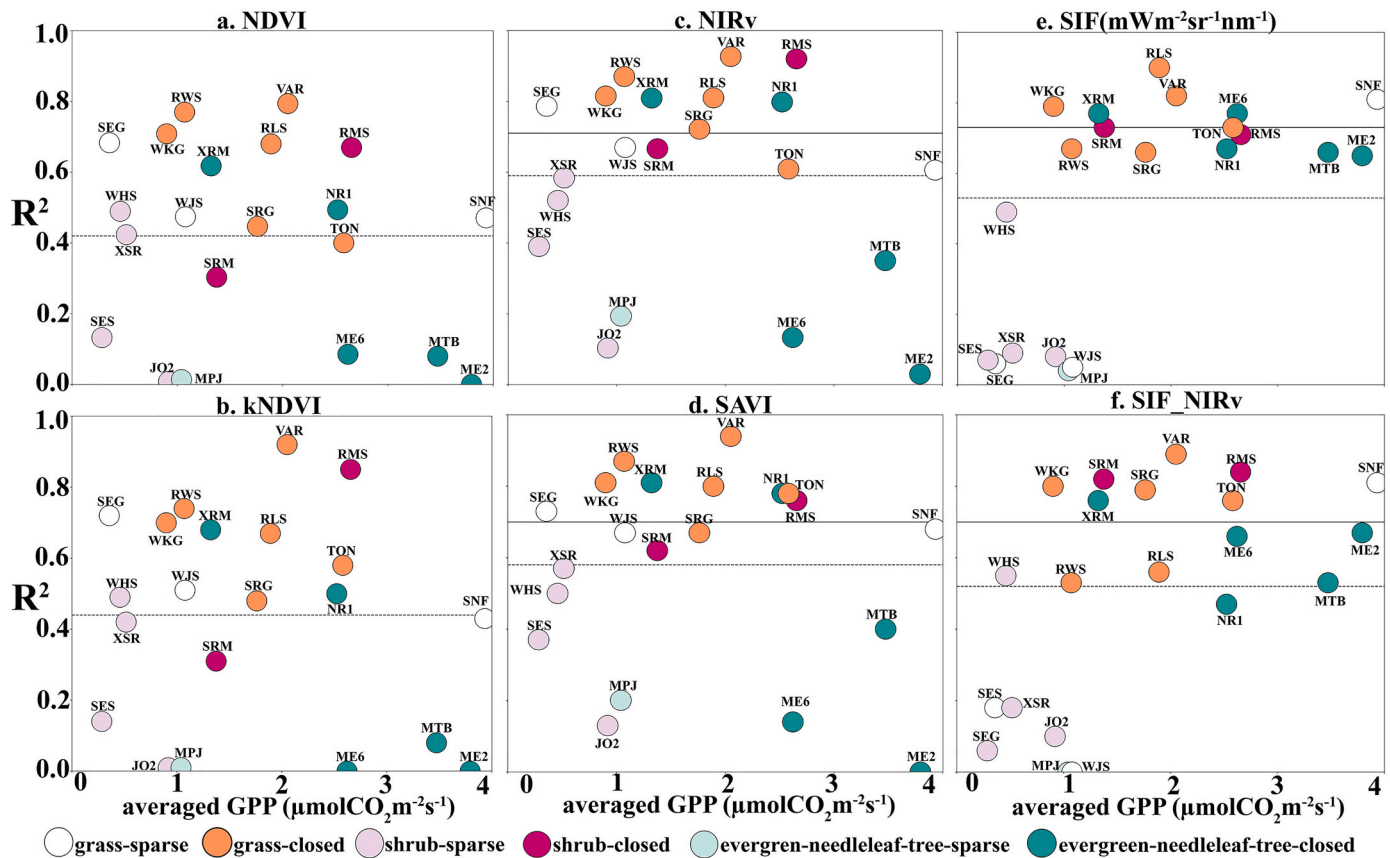


Fig. 3. The coefficient of determination (R^2) for 21 dryland EC sites derived from monthly GPP and monthly satellite proxies plotted against the mean GPP measured at the site over the full study period. Comparison of EC GPP and (a) NDVI (1.5-km²), (b) kNDVI (1.5-km²), (c) NIR_v (1.5-km²), (d) SAVI (1.5-km²), (e) SIF (16-km²) and (f) SIF_NIR_v (1.5-km²) are colour coded by grass-sparse, grass-closed, shrub-sparse, shrub-closed, evergreen-needleleaf-tree-sparse, and evergreen-needleleaf-tree-dominated sites. The dashed lines denote the means of the R^2 values of all sites. The solid lines denote the mean R^2 when excluding all evergreen-needleleaf-tree sites for NIR_v and SAVI, and all sparse sites for SIF and SIF_NIR_v.

1.5-km² and 16-km² grid using 30-m rangeland cover v2.0 data (<http://rangelands.app/>).

For the across-site analyses, we used daily GPP, NDVI, kNDVI, NIR_v, SAVI, SIF, and SIF_NIR_v at each site over the 21-month (full record) study period from April 2018 to December 2019 as inputs into vegetation class-specific linear regression models. To investigate seasonal dynamics, we calculated approximately monthly (± 14 -days moving window) mean time series as inputs to EC site-specific linear regression models. To better evaluate proxy performance at EC sites, across which all proxies were relatively well correlated with seasonal GPP dynamics ($R^2 > 0.4$), we further analyzed the seasonal bias in the proxy: GPP relationship. We focused six grass-dominant sites plus sc-SRM with mixed grass and woody covers (grass >28%, Ratio 1 < 50%, Table S2), we reported the seasonal bias for each proxy as the average of residuals from each linear fit during pre- and post-peak periods that were defined by the timing of peak GPP during the major growing season in both 2018 and 2019. Note sc-SRM is here defined as shrub-closed (similar to other sources) but has nearly identical grass and woody covers ($\sim 28\%$ each), which justifies its inclusion in this analysis. We then plotted the absolute values of the seasonal biases for two categories of woody vegetation (shrub+tree) fraction ((0, 30%), (30%,50%)) to understand the influence of woody cover on seasonal biases across grass-dominant sites. We additionally calculated these seasonal biases at weekly (± 4 -days moving window) and biweekly (± 7 -days moving window) scales to assess their sensitivity to temporal scale. We excluded shrub- and tree-dominated sites from this hysteresis analysis since only two sites from each category satisfied criteria for these analyses.

3. Results

3.1. Across-site spatial evaluation of dryland GPP proxies

All proxies captured the across-site spatial variability of GPP, with R^2 values ranging from 0.69 for kNDVI to 0.79 for NIR_v (Fig. 2). NDVI and kNDVI (Fig. 2a, b), NIR_v and SAVI (Fig. 2c, d), SIF and NIR_v-downscaled SIF (SIF_NIR_v) (Fig. 2e, f) performed strikingly similarly in their ability to capture GPP across ecosystem types. Notably, compared to the four spectral reflectance-based indices, the SIF:GPP and SIF_NIR_v:GPP relationship appeared to vary as a function of ecosystem type. For example, for SIF:GPP, the slope of the relationship across evergreen-needleleaf-tree-dominant sites ($32.0 \mu\text{mol CO}_2 \text{ m}^{-2} \text{ s}^{-1} / \text{mW m}^{-2} \text{ nm}^{-1} \text{ sr}^{-1}$) was more than double the slope of the relationship across grass-dominated sites ($13.2 \mu\text{mol CO}_2 \text{ m}^{-2} \text{ s}^{-1} / \text{mW m}^{-2} \text{ nm}^{-1} \text{ sr}^{-1}$) (Fig. 2e, f).

3.2. Within-site seasonal evaluation of dryland GPP proxies

3.2.1. Reflectance-based proxies: NDVI, kNDVI, NIR_v, and SAVI

The monthly NDVI:GPP relationship across all sites (mean $R^2 = 0.41$) was the lowest of all the reflectance-based indices (Fig. 3a). Specifically, NDVI had the lowest average R^2 in grass-dominated (mean $R^2 = 0.60$), shrub-dominated (mean $R^2 = 0.31$), and evergreen-needleleaf-tree-dominated (mean $R^2 = 0.22$) sites. The correlation between NDVI and GPP was insensitive to temporal aggregation at weekly, biweekly, and monthly time scales (Figs. 3a, S2a, S2b). The monthly kNDVI:GPP relationship across all sites (mean $R^2 = 0.43$) was strikingly similar to the NDVI:GPP relationship (Fig. 3b), though R^2 at grass- and shrub-

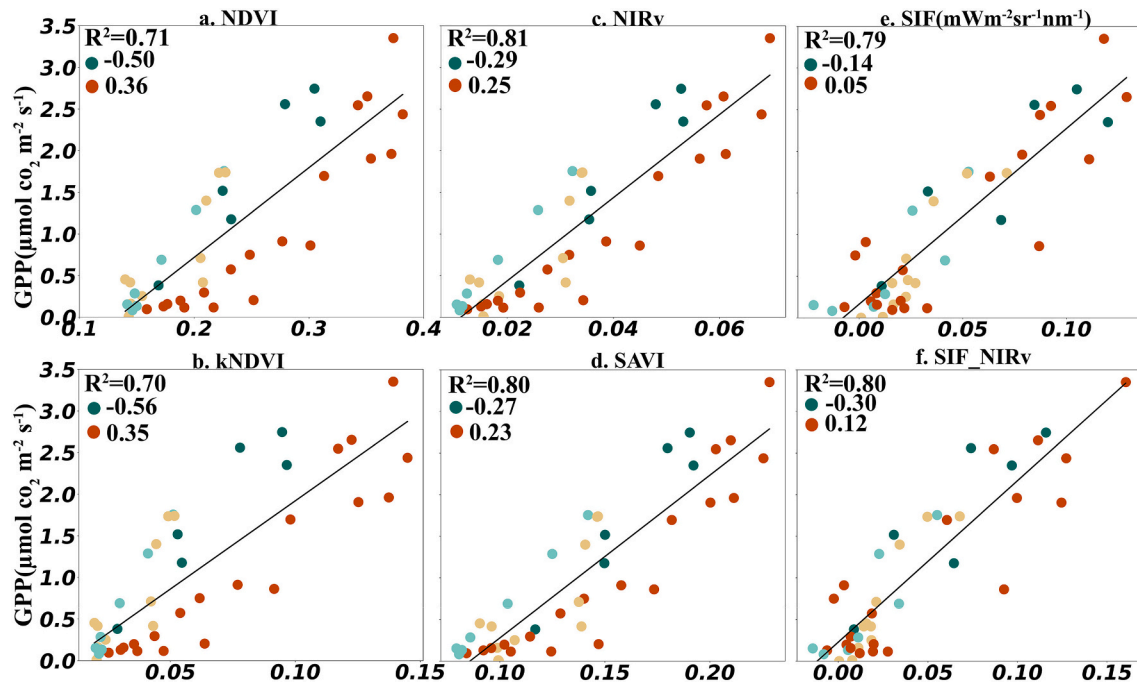


Fig. 4. The relationship between EC GPP and satellite NDVI(a), kNDVI(b), NIRv(c), SAVI(d), SIF(e), and SIF NIRv(f) for a representative closed grassland site (gc-WKG; 23% fractional woody cover). Green and brown circles represent the pre-peak and post-peak periods, respectively. Seasonal biases were calculated as the mean of the residuals from each linear fit during pre-peak and post-peak periods as reported in the legend. Gc-WKG was characterized by bi-modal growing seasons during both 2018 and 2019 and pre-peak and post-peak bias is reported for both periods; light green and light brown dots represent the first growing season and dark green and orange dots represent the second growing season. (For interpretation of the references to colour in this figure legend, the reader is referred to the web version of this article.)

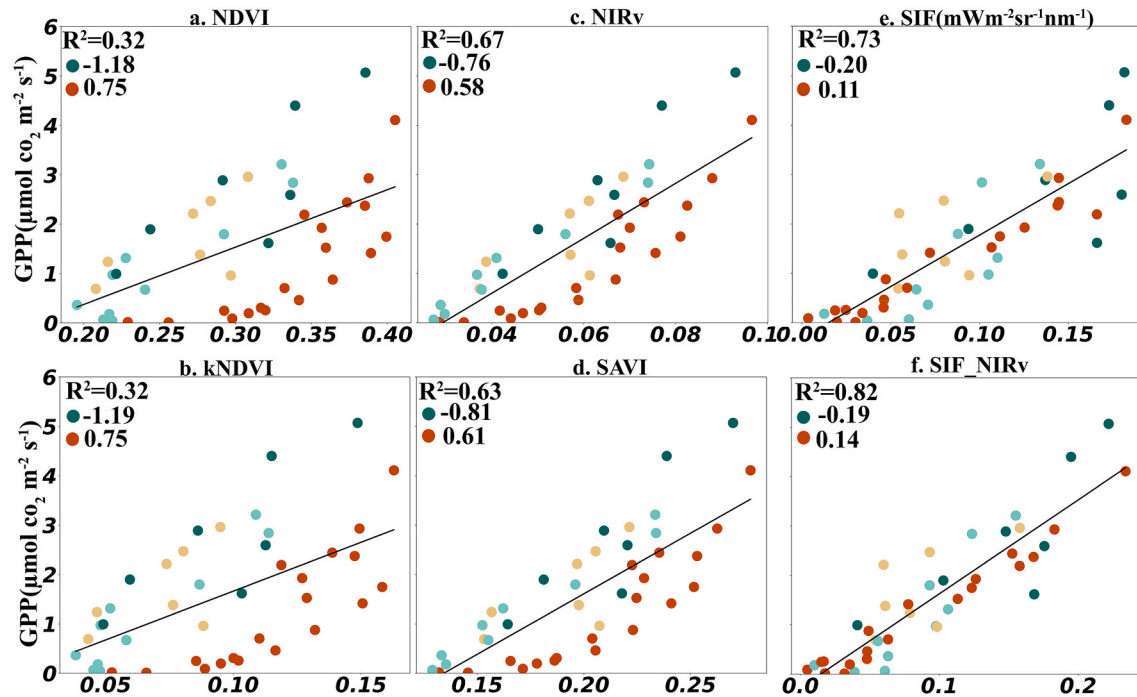


Fig. 5. The relationship between EC GPP and satellite NDVI(a), kNDVI(b), NIRv(c), SAVI(d), SIF(e), and SIF NIRv(f) for a representative closed shrubland site (sc-SRM; 50% fractional woody cover). Green and brown circles represent the pre-peak and post-peak periods, respectively. Seasonal biases were calculated as the mean of the residuals from each linear fit during pre-peak and post-peak periods as reported in the legend. Sc-SRM was characterized by bi-modal growing seasons during both 2018 and 2019 and pre-peak and post-peak bias is reported for both periods; light green and light brown dots represent the first growing season and dark green and orange dots represent the second growing season. (For interpretation of the references to colour in this figure legend, the reader is referred to the web version of this article.)

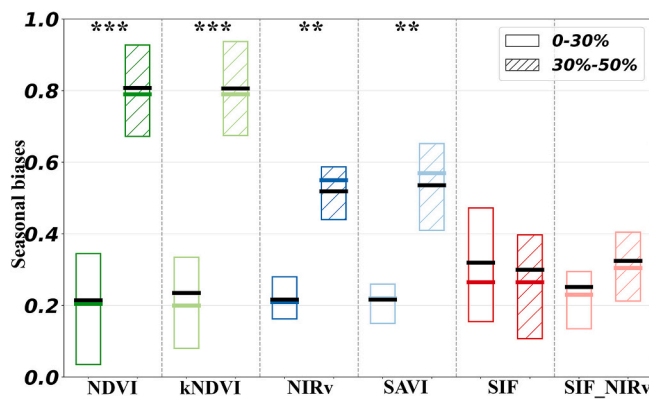


Fig. 6. Seasonal biases in the monthly NDVI:GPP, kNDVI:GPP, NIRv:GPP, SAVI:GPP, SIF:GPP and SIF_NIRv:GPP relationships across two fractional woody (shrub+tree) cover classes (0–30% and 30%–50%). Seasonal biases represent the absolute value of averaged residuals of the linear regression fit during pre- and post-season (Table S3). Fractional shrub and tree cover is defined according to Ratio 1 [(shrub+tree) / total vegetation] (Table S2). “***” denotes significant differences between paired distributions based on a standard ANOVA test with $p < 0.001$. “**” denotes significant differences between paired distributions based on a standard ANOVA test with $p < 0.01$. The bars represent the 25th–50th–75th percentile of the data points in each relationship; the black lines represent the means of seasonal bias in each relationship.

dominated sites was slightly higher for kNDVI (mean $R^2 = 0.64$ and 0.37 , respectively) relative to NDVI (mean $R^2 = 0.60$ and 0.31 , respectively).

The monthly NIRv:GPP relationship across all sites (mean $R^2 = 0.57$) was improved across all vegetation classes relative to NDVI and kNDVI (Fig. 3c). Notably, the NIRv:GPP relationship was relatively low across the evergreen-needleleaf-tree- and evergreen-shrub-dominated sites (ns-MPJ, nc-VCP, nc-ME6, nc-MTB, nc-ME2, and ss-Jo2), with R^2 ranging from 0.02 to 0.35 (Fig. 3c). Excluding evergreen-dominated sites, the NIRv:GPP relationship increased significantly (mean $R^2 = 0.71$). NIRv performed best as an indicator of monthly GPP in grass-closed and shrub-closed sites (mean $R^2 = 0.79$). The correlation between NIRv and GPP was insensitive to temporal aggregation at weekly, biweekly, and monthly time scales (Fig. 3c, S2c, S2d). The monthly SAVI:GPP relationship across all sites (mean $R^2 = 0.57$) was strikingly similar to the NIRv:GPP relationship (Fig. 3d).

Across seven grass-closed sites, the relationship between reflectance-based proxies (i.e., NDVI, kNDVI, NIRv, and SAVI) and GPP was characterized by significant seasonal hysteresis, which we defined as the averaged bias in the relationships during the pre- and post-peak periods (Table S3). For example, pre-peak biases were -0.50 and $-1.18 \mu\text{mol CO}_2 \text{ m}^{-2} \text{ s}^{-1}$ and post-peak biases were 0.36 and $0.75 \mu\text{mol CO}_2 \text{ m}^{-2} \text{ s}^{-1}$ in the monthly NDVI:GPP relationship at gc-WKG (Fig. 4) and sc-SRM (Fig. 5), respectively. These seasonal hysteresis effects were significantly larger at sites with 30–50% fractional woody plant cover (e.g., sc-SRM) than at sites with 0–30% fractional woody plant cover (e.g., gs-WKG) (Figs. 4–6). Across all sites, the seasonal hysteresis of the NDVI:GPP relationship (mean bias = 0.27 and $0.97 \mu\text{mol CO}_2 \text{ m}^{-2} \text{ s}^{-1}$ for 0–30% and 30%–50% woody cover, respectively) was again similar to the kNDVI:GPP relationship (mean bias = 0.24 and $0.81 \mu\text{mol CO}_2 \text{ m}^{-2} \text{ s}^{-1}$ for 0–30% and 30%–50% woody cover, respectively) (Fig. 6). Notably, the seasonal NIRv:GPP and SAVI:GPP hysteresis estimates were also strikingly similar and less pronounced than the NDVI:GPP and kNDVI:GPP hysteresis estimates (Figs. 4–6). For example, pre-peak biases were reduced to -0.29 and $-0.76 \mu\text{mol CO}_2 \text{ m}^{-2} \text{ s}^{-1}$ and post-peak biases were reduced to 0.25 and $0.58 \mu\text{mol CO}_2 \text{ m}^{-2} \text{ s}^{-1}$ in the monthly NIRv:GPP relationship at gc-WKG (Fig. 4) and sc-SRM (Fig. 5), respectively. The NDVI:GPP, kNDVI:GPP, NIRv:GPP, and SAVI:GPP relationships and their seasonal hysteresis characters were insensitive to

temporal aggregation at weekly, biweekly, and monthly time scales (Figs. 3, 6, S2, S3).

3.2.2. SIF and SIF_NIRv

The correlation between monthly SIF and monthly GPP across most sites (mean $R^2 = 0.53$) and all vegetation classes was improved relative to NDVI (Fig. 3e). Notably, the seasonal relationship between SIF and GPP was relatively weak (mean $R^2 = 0.13$) across low-productivity sites characterized by average $\text{GPP} < 1 \mu\text{mol CO}_2 \text{ m}^{-2} \text{ s}^{-1}$ and significant bare ground relative to vegetation coverage (Ratio 2 > 0.2), including gs-SEG, gs-WJS, ss-WHS, ss-JO2, ss-SES, ss-XSR and ns-MPJ (Fig. 3e, Table S2). Also, unlike the four reflectance-based proxies, temporal aggregation had a large effect on the strength of the SIF:GPP relationship, with correlation values increasing from weekly to monthly time scales (Figs. 3e, S2e, S2f). After excluding sparse sites, the monthly SIF:GPP relationship increased (mean $R^2 = 0.74$). The SIF:GPP relationship had low seasonal hysteresis, with pre-peak biases of -0.14 and -0.20 and post-peak biases of 0.05 and $0.11 (\mu\text{mol CO}_2 \text{ m}^{-2} \text{ s}^{-1})$ for gs-WKG and sc-SRM respectively (Figs. 4–5). Notably, seasonal biases were not significantly different between the two classes of woody (tree+shrub) fractional cover and these findings were preserved at monthly, biweekly, and weekly timescale (Figs. 6, S3). Compared to the SIF:GPP relationship, the SIF_NIRv:GPP seasonal R^2 values were lower across all evergreen-needleleaf-tree sites but slightly higher and with reduced seasonal biases at six out of eight non-evergreen, high-productivity sites (Figs. 3–6, S3).

4. Discussion

4.1. Across-site spatial evaluation of dryland GPP proxies

All satellite-based proxies captured across-site spatial variability of GPP reasonably well across sites classified by dominant functional types (Fig. 2). NDVI and kNDVI performed strikingly similarly, as did NIRv and SAVI, in their ability to capture GPP across sites. We note, however, that we applied the default nonlinear sensitivity factor (σ) and soil brightness correction factor (L) for kNDVI and SAVI, respectively. There remains a need for future research that explores the sensitivity of these indices to their respective correction factors (Zhao et al., 2018; Camps-Valls et al., 2021).

We found that the SIF:GPP relationship was relatively sensitive to ecosystem type, with improved correlation when ecosystem types were separated (Fig. 2). Two potential explanations for the observed ecosystem-specific sensitivities of SIF:GPP include: 1) differential SIF emission and scattering due to differences in canopy structures (Migliavacca et al., 2017; Qiu et al., 2019; Dechant et al., 2020); and 2) differential SIF emission per unit CO_2 uptake driven by variation in the dominant photosynthetic pathways (C3 vs. C4) (He et al., 2020). Notable, the C3-grass-dominated sites had relatively lower SIF:GPP slopes compared to all other sites, possibly due to higher rates of photorespiration in the C3 photosynthetic pathway (Fig. S4; Chu et al., 2021). However, the C3-evergreen-needleleaf-tree-dominated sites had the highest SIF:GPP slopes, which suggests that structure and re-absorption of SIF emissions may also play a dominant role in SIF:GPP relationship (Fig. S4). Future research is needed to more thoroughly understand and separate the physiological and structural factors that mediate the SIF:GPP relationship.

4.2. Within-site seasonal evaluation of dryland GPP proxies

NIRv and SIF outperformed all other proxies in their ability to track seasonal GPP dynamics (Fig. 3), consistent with previous studies focused on the western US (Smith et al., 2018; Zuromski et al., 2018), Australian drylands (Wang et al., 2019), and African savannas (Mengistu et al., 2020). At low-productivity sites, e.g., grass-sparse and shrub-sparse sites (gs-WJS, gs-SEG, ss-WHS, and ss-XSR), NIRv consistently outperformed

SIF at capturing seasonal GPP variation (Fig. 3, Table S4). NIR_v was largely successful in isolating the vegetation signal from the confounding effects of soil brightness (Templeton et al., 2014; Badgley et al., 2019; Baldocchi et al., 2020) as demonstrated by its close correlation with SAVI (Fig. 3). SIF performed relatively poorly at capturing seasonal GPP dynamics at low-productivity sites, likely due to the low signal-to-noise ratio of SIF retrievals (Guanter et al., 2015; Köhler et al., 2021). In other words, at low productivity sites, the true SIF signal is likely too weak to overcome the inherent noise associated with the SIF retrieval (Köhler et al., 2021), resulting in very low correlation with seasonal GPP dynamics. We also found evidence of low SIF signal-to-noise ratios during non-growing season periods at high-productivity sites (gc-SRG, gc-VAR, gc-TON, gc-RWS, and sc-RMS), resulting in large apparent pre- and post-peak biases (Fig. S5). Further sensitivity analysis in which the temporal resolution was increased from monthly to weekly revealed that SIF:GPP R^2 values were generally reduced (Figs. 3e, S2e, S2f) and SIF:GPP seasonal biases were general increased relative to the reflectance-based proxies (Figs. 6, S3). This relatively high sensitivity to temporal scale suggests that satellite SIF observations are more susceptible to noise at these higher frequencies than reflectance-based proxies. Other factors including SIF signal re-absorption and sun-sensor geometry could also drive noise in the SIF:GPP relationship and should be the focus of future research efforts (Romero et al., 2018; Hao et al., 2020; Hao et al., 2021; Chu et al., 2021).

At closed evergreen-needleleaf-tree-dominated sites, SIF captured more seasonal GPP variability ($R^2 = 0.70$) than NIR_v ($R^2 = 0.42$) (Fig. 3, Table S4). This is consistent with previous research finding that SIF captures more than just seasonal changes in vegetation greenness and potentially contains more information related to physiological function (e.g., photosynthetic rate, stomatal regulation, photochemical quenching, etc.) (Joiner et al., 2014; Walther et al., 2016; Magney et al., 2019). These relatively high correlations persist despite the coarser spatial resolution of TROPOMI SIF observations, which is an order of magnitude larger than typical EC tower footprints (Chu et al., 2021). While, we minimized the impact of this spatial mismatch by filtering TROPOMI SIF observations to include only the vegetation cover types associated with a given EC tower, it is likely that this simple filtering was inadequate in some cases, especially for sites with relatively high heterogeneity around the EC tower site. Downscaling SIF by NIR_v observations was attempted to better account for this spatial mismatch, but instead seemed to transfer the existing limitations of NIR_v for tracking GPP seasonal variability (Fig. 3), and thus SIF alone outperformed $\text{SIF}_{\text{NIR}_v}$ at evergreen-needleleaf-tree sites (Fig. 3, Table S4). More accurate monitoring of heterogeneous dryland regions will require higher resolution SIF observations that better isolate the signals of mixed vegetation functional types (Smith et al., 2019). NIR_v did perform relatively well and similar to SIF at two neighboring evergreen forest sites: Niwot Ridge Forest and Rocky Mountain National Park (nc-NR1 and nc-XRM, Fig. 3). This finding is potentially explained by previous work demonstrating that seasonal changes in canopy colour, which can be tracked with reflectance-based proxies, correlate with seasonal GPP for these ecosystems (Wu et al., 2014; Seyedinrollah et al., 2020).

SIF downscaled by NIR_v ($\text{SIF}_{\text{NIR}_v}$) slightly improved seasonal GPP estimates and reduced seasonal bias relative to SIF alone at most grass-closed and shrub-closed sites (Figs. 3, 6, Tables S3, S4). At these sites, the higher spatial resolution of NIR_v observations likely helped to reduce noise inherent in the SIF signal and associated with footprint mismatch (Turner et al., 2020). However, at low productivity sites (mean GPP $< 1 \mu\text{mol CO}_2 \text{ m}^{-2} \text{ s}^{-1}$) with significant bare ground cover, the SIF signal was too weak to overcome random noise in the retrieval, resulting in the NIR_v observations outperforming $\text{SIF}_{\text{NIR}_v}$ (Fig. 3, Table S4). This finding is consistent with recent work showing that $\text{SIF}_{\text{NIR}_v}$ explained less than 10% of GPP variability at shrub and savanna EC tower sites (Chu et al., 2021). Here, by incorporating fractional land cover data within a 1.5-km² and 16-km² grid at each EC site, we provide new evidence that the signal-to-noise of the SIF retrieval is sensitive to

fractional bare ground cover when the surface is brighter than vegetation (Guanter et al., 2015), which is a common issue across drylands (Huete, 1988; Gholami Baghi and Oldeland, 2019). Other methods, such as machine learning (Gentine and Alemohammad, 2018) or a semi-empirical downscaling based on light use efficiency (Duveiller et al., 2020), should be explored in the future to build upon the respective strengths of NIR_v and SIF while limiting their weaknesses.

4.3. Reflectance-based GPP proxies are prone to seasonal hysteresis

While NIR_v and SIF accurately captured seasonal GPP across grass-closed sites with mixed grass and woody cover, we found significant patterns of seasonal hysteresis in the correlations between GPP and reflectance-based vegetation proxies (NDVI, kNDVI, NIR_v , and SAVI) from weekly to monthly scale (Figs. 4–6, S3, Table S3). These patterns differed depending on the proportion of evergreen shrubs and trees in the tower footprint (Figs. 6, S3), suggesting that reflectance-based proxies are seasonally decoupled from GPP for these vegetation types. In other words, evergreen vegetation maintained the appearance of high photosynthetic capacity (i.e., remains green) even during periods of low GPP (Smith et al., 2018; Yan et al., 2019; Knowles et al., 2020). Thus, it is important to account for spatially heterogeneous mixtures of these functional types when using reflectance-based proxies as GPP proxies or inputs of GPP models. SIF was much less impacted by this type of seasonal bias and thus represents an improved proxy for seasonal variability of GPP in many dryland ecosystems, especially at the end of the growing season (Figs. 6, S3; Wang et al., 2020b).

Seasonal hysteresis in the relationships between reflectance-based proxies and GPP could also be impacted by changing soil brightness during pre- and post-peak periods (Gitelson et al., 2014; Flanagan et al., 2015; Nestola et al., 2016; Peng et al., 2017). For example, at low productivity sites like gs-SEG and gs-WJS with more than 30% bare ground coverage (Fig. S6, Table S3–1), the bare ground fraction likely changes throughout the growing season as bare ground fills in with annual cover species and this could also contribute to seasonal hysteresis effects. However, across closed canopy sites with high productivity and less than 20% bare ground coverage, we find evidence that seasonal hysteresis with GPP is driven by differences in the herbaceous and woody vegetation fractions (Figs. 6, S3). This idea is supported by our findings at gc-WKG and sc-SRM sites with potentially two growing seasons, where the seasonal hysteresis with GPP mostly occurs during the second (dominant) growing season when bare ground coverage is minimized (Figs. 4–5). Similarly, changes in nitrogen content, chlorophyll content, and vegetation structure between the pre- and post-peak periods might also contribute to seasonal hysteresis (Gitelson et al., 2014; Flanagan et al., 2015; Nestola et al., 2016; Peng et al., 2017). Notably, the NIR_v :GPP relationship showed less seasonal hysteresis compared to NDVI:GPP likely due to its reduced sensitivity to background soil brightness (Huete, 1988; Badgley et al., 2017), and increased sensitivity to ecosystem structure (Table S3; Peng et al., 2017).

Seasonal hysteresis between reflectance-based proxies and GPP also differed across climate zones. At the Mediterranean California sites (gc-TON and gs-SNF), reflectance-based vegetation proxies (NDVI, kNDVI, NIR_v , and SAVI) overestimated GPP prior to the annual peak but underestimated it thereafter (Table S3–1). However, at the North American Monsoon-affected sites (the summer rainfall-dominated sites of gs-WJS, gs-SES, gc-WKG, gc-SRG, and sc-SRM), the hysteresis pattern between reflectance-based vegetation proxies and GPP was reversed (Table S3–1). At the Mediterranean-climate sites in California, the understory grasses distinctly green up during the cool, wet season from October to April, but energy limits GPP during the winter, resulting in greenness increasing ahead of GPP. In late spring, the shallow soil dries, understory grasses brown, and greenness declines, but the overstory oaks thrive on deeper soil moisture such that GPP stays elevated (Bartolome, 1979; Xu and Baldocchi, 2003; Ma et al., 2007; Liu et al., 2017). In contrast, at Monsoon-affected sites, both grasses and shrubs green up

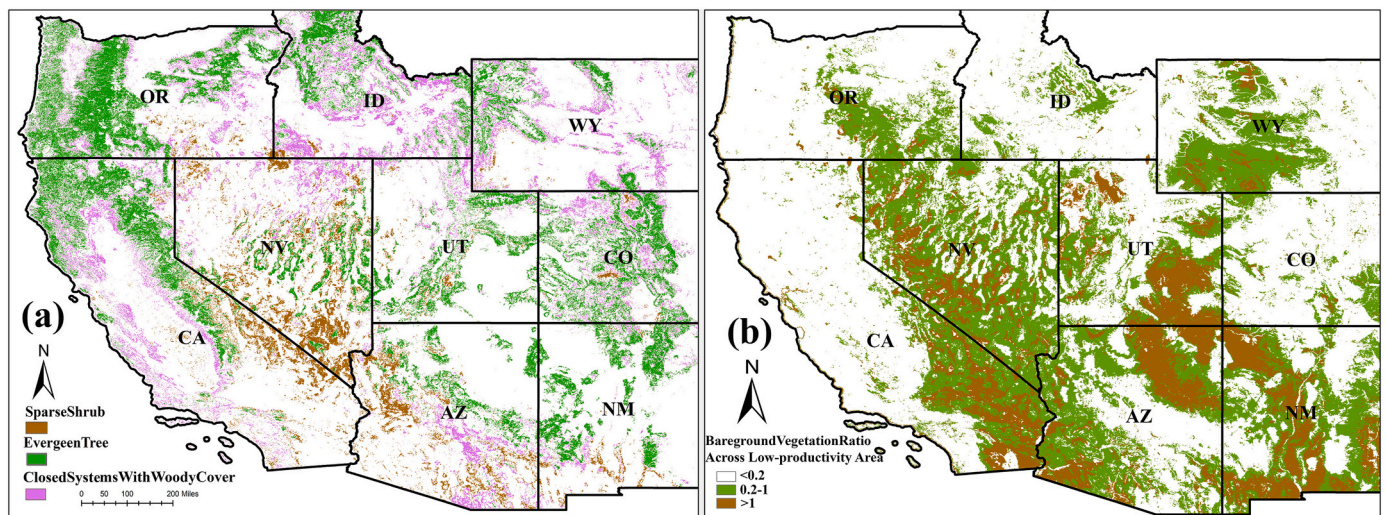


Fig. 7. Areas in the semi-arid western US where (a) TROPOMI SIF would be expected to outperform MODIS NDVI/NIR_v and (b) MODIS NDVI/NIR_v would be expected to outperform TROPOMI SIF at estimating GPP seasonal dynamics. (a) Purple pixels are grass-closed regions with significant tree covers (30% to 50%), green pixels are dominated by evergreen trees, and grey pixels are dominated by sparse shrubs. (b) The low-productivity regions (colored pixels) are defined as average GPP < $\sim 1 \mu\text{mol CO}_2 \text{ m}^{-2} \text{ s}^{-1}$ (or averaged NIR_v < 0.04,) where the ratio between bare ground and vegetation coverage is greater than 0.2. (For interpretation of the references to colour in this figure legend, the reader is referred to the web version of this article.)

and photosynthesize during spring using stored winter moisture. Following the second, dominant growing season driven by summer rainfall, overstory shrubs and trees can remain green for weeks to months after soil moisture is depleted and GPP falls (Scott et al., 2009; Barron-Gafford et al., 2017; Yan et al., 2019).

4.4. Complementary application of reflectance-based proxies and SIF observations across dryland ecosystems

The reflectance-based proxies considered here estimated seasonal GPP dynamics relatively well in homogeneous and non-evergreen areas but poorly in heterogeneous and/or evergreen regions. On the contrary, SIF performed well in high-productivity regions and poorly in low-productivity regions. These differences in skill are often complementary and can be potentially leveraged to more accurately characterize GPP dynamics across much of the western US. Based on the current analysis, we estimate that 25% of the semi-arid western US land area corresponds to heterogeneous or evergreen regions (Fig. 7a), which will induce bias when using reflectance-based proxies to estimate seasonal GPP. This area specifically includes 13% evergreen-dominated regions, where reflectance-based proxies failed to capture seasonal GPP dynamics; 8% grass-closed regions with more than 30% woody cover, where reflectance-based proxies had seasonally hysteretic relationships to GPP; and 4% sparse shrub regions, where NIR_v only captured around 50% of the variance in seasonal GPP dynamics (Fig. 7a). In contrast, TROPOMI SIF failed to accurately estimate seasonal GPP across low productivity areas that account for 39% of the semi-arid western US (Fig. 7b). These results underscore the importance of functional heterogeneity in dryland ecosystems and demonstrate that generalizing across regions using a single vegetation proxy, whether with a process-based or empirical model, will likely result in inaccurate and/or biased GPP estimates (Smith et al., 2019). Taken together, our findings indicate that different vegetation proxies are better suited for different dryland ecosystem types, and suggest that data integration approaches, particularly those focused on integrating SIF and NIR_v observations, are critical to improved performance of satellite-based GPP models across drylands from the region to the globe.

5. Conclusions

Accurate detection of seasonal to interannual variability of GPP in drylands is complicated in part by the highly heterogeneous mixtures of bare ground, grass, shrubs, and trees characteristic of dryland ecosystems. Here, we evaluated the skill of NDVI, kNDVI, NIR_v, SAVI, SIF, and SIF_NIR_v to predict GPP dynamics as measured by 21 eddy covariance tower sites across six major dryland classes: grass-sparse, grass-closed, shrub-sparse, shrub-closed, evergreen-needleleaf-tree-sparse, and evergreen-needleleaf-tree-closed of the western US. NIR_v and SIF were found to perform best in capturing both spatial patterns and seasonal dynamics of GPP, and further captured complementary aspects of seasonal GPP dynamics: NIR_v was the best GPP proxy across non-evergreen vegetation-sparse sites, while SIF was the best GPP proxy across evergreen and closed-canopy sites. We also found significant seasonal bias and hysteresis in the relationships between the reflectance-based proxies considered here and GPP as a function of increasing fractional shrub and tree coverage across grass-dominated sites. Based on our findings, NIR_v likely has significant limitations for approximating GPP across 25% of the western US (high heterogeneity and/or evergreen vegetation), while SIF has significant limitations for approximating GPP across 39% of the western US (low productivity sites with a significant portion of bare ground). Our research indicates that use of a single proxy or method to characterize vegetation dynamics across dryland areas will likely result in biased estimates of GPP in at least one part of the growing season. We suggest careful consideration of vegetation heterogeneity when integrating different proxies or methods for improved representation of vegetation dynamics across dryland regions.

Declaration of Competing Interest

The authors declare that they have no known competing financial interests or personal relationships that could have appeared to influence the work reported in this paper.

Acknowledgements

We thank Brady W. Allred for providing constructive feedback on an early version of this manuscript. X.W. acknowledges funding from NASA Future Investigators (grant 80NSSC19K1335). W.K.S. acknowledges

support from NASA CCS (grant 80NSSC21K1709). W.K.S. and M.P.D. acknowledge support from NASA SMAP (grant 80NSSC20K1805). W.K.S. and S.C.R. acknowledge support from the US Geological Survey Community for Data Integration (cooperative agreement G19AC00424) and the Department of Defense SERDP (grant RC18-1322). W.K.S. and W.J.P. acknowledge support from the United States Department of Agriculture CDI (cooperative agreement 58-3050-9-013 and 58-0111-17-013). MODIS surface reflectance (MCD43A4) data used here are available via <https://lpdaac.usgs.gov/products/mcd43a4v006/>. TROPOMI SIF data used here are available via <ftp://fluo.gps.caltech.edu/data/tropomi/ungridded/>. Eddy covariance half-hour observations of the net ecosystem exchange of CO₂ are available via ameriflux.lbl.gov through funding from the U.S. Department of Energy's Office of Science. Vegetation fractional cover data are available via <https://rangelands.app/>. Any use of trade, firm, or product names is for descriptive purposes only and does not imply endorsement by the U.S. Government.

Appendix A. Supplementary data

Supplementary data to this article can be found online at <https://doi.org/10.1016/j.rse.2021.112858>.

References

- Ahlstrom, A., Raupach, M., Schurgers, G., Smith, B., Arneeth, A., Jung, M., et al., 2015. The dominant role of semi-arid ecosystems in the trend and variability of the land CO₂ sink. *Science* 348, 895–899.
- Allred, B.W., Bestelmeyer, B.T., Boyd, C.S., Brown, C., Davies, K.W., Ellsworth, L.M., Erickson, T.A., Fuhlendorf, S.D., Griffiths, T.V., Jansen, V., Jones, M.O., Karl, J., Maestas, J.D., Maynard, J.J., McCord, S.E., Naugle, D.E., Starns, H.D., Twidwell, D., Uden, D.R., 2020. Improving Landsat Predictions of Rangeland Fractional Cover with Multitask Learning and Uncertainty. *bioRxiv*:2020.06.10.142489. <https://doi.org/10.1101/2020.06.10.142489>.
- Badgley, G., Field, C.B., Berry, J.A., 2017. Supplementary materials canopy near-infrared reflectance and terrestrial photosynthesis. *Sci. Adv.* 3, 1602244. <https://doi.org/10.1126/sciadv.1602244>.
- Badgley, G., Anderegg, L.D.L., Berry, J.A., Field, C.B., 2019. Terrestrial gross primary production: using NIR V to scale from site to globe. *Glob. Chang. Biol.* 1–10 <https://doi.org/10.1111/gcb.14729>.
- Baldocchi, D.D., Ryu, Y., Dechant, B., Eichelmann, E., Hemes, K., Ma, S., et al., 2020. Outgoing near-infrared radiation from vegetation scales with canopy photosynthesis across a spectrum of function, structure, physiological capacity, and weather. *J. Geophys. Res. Biogeosci.* 125 <https://doi.org/10.1029/2019JG005534> e2019JG005534.
- Barron-Gafford, G.A., Sanchez-Cañete, E.P., Minor, R.L., Hendryx, S.M., Lee, E., Sutter, L. F., Tran, N., Parra, E., Colella, T., Murphy, P.C., Hamerlynck, E.P., Kumar, P., Scott, R.L., 2017. Impacts of hydraulic redistribution on grass–tree competition vs. facilitation in a semi-arid savanna. *New Phytol.* 215, 1451–1461. <https://doi.org/10.1111/nph.14693>.
- Bartolome, J.W., 1979. Germination and seedling establishment in California annual grassland. *J. Ecol.* 273–281.
- Biederman, J.A., Scott, R.L., Bell, T.W., Bowling, D.R., Dore, S., Garatuza-Payan, J., Kolb, T.E., Krishnan, P., Krofcheck, D.J., Litvak, M.E., Maurer, G.E., Meyers, T.P., Oechel, W.C., Papuga, S.A., Ponce-Campos, G.E., Rodriguez, J.C., Smith, W.K., Vargas, R., Watts, C.J., Yezpe, E.A., Goulden, M.L., 2017. CO₂ exchange and evapotranspiration across dryland ecosystems of southwestern North America. *Glob. Chang. Biol.* 23, 4204–4221. <https://doi.org/10.1111/gcb.13686>.
- Bodesheim, P., Jung, M., Gans, F., Mahecha, M., Reichstein, M., 2018. Upscaled diurnal cycles of land-atmosphere fluxes: a new global half-hourly data product. *Earth Syst. Sci. Data Discuss.* 1–47. <https://doi.org/10.5194/essd-2017-130>.
- Brandt, M., Tucker, C.J., Kariyana, A., Rasmussen, K., Abel, C., Small, J., Chave, J., Rasmussen, L.V., Hiernaux, P., Diouf, A.A., Kergoat, L., Mertz, O., Igel, C., Gieseke, F., Schöning, J., Melocik, K., Meyer, J., Sinno, S., Montagu, A., Dendoncker, M., Fensholt, R., 2020. An unexpectedly large count of non-forest trees in the western Sahara and Sahel. *Nature*. <https://doi.org/10.1038/s41586-020-2824-5>.
- Camps-Valls, G., et al., 2021. A unified vegetation index for quantifying the terrestrial biosphere. *Sci. Adv.* 1–11.
- Chu, et al., 2021. Representativeness of Eddy-Covariance flux footprints for areas surrounding AmeriFlux sites. *Agric. For. Meteorol.* 301–302, 108350 <https://doi.org/10.1016/j.agrformet.2021.108350>.
- Dechant, B., Ryu, Y., Badgley, G., Zeng, Y., Berry, J.A., Zhang, Y., Goulas, Y., Li, Z., Zhang, Q., Kang, M., Li, J., Moya, I., 2020. Canopy structure explains the relationship between photosynthesis and sun-induced chlorophyll fluorescence in crops. *Remote Sens. Environ.* 241 <https://doi.org/10.1016/j.rse.2020.111733>.
- Dewitz, J., 2019. National Land Cover Database (NLCD) 2016 Products (ver. 2.0, July 2020): U.S. Geological Survey Data Release. <https://doi.org/10.5066/P96HHBIE>.
- Doughty, R., Köhler, P., Frankenberg, C., Magney, T.S., Xiao, X., Qin, Y., Wu, X., Moore, B., 2019. TROPOMI reveals dry-season increase of solar-induced chlorophyll fluorescence in the Amazon forest. *Proc. Natl. Acad. Sci. U. S. A.* 116, 22393–22398. <https://doi.org/10.1073/pnas.1908157116>.
- Duveiller, G., Filippini, F., Walther, S., Köhler, P., Frankenberg, C., Guanter, L., Cescatti, A., 2020. A spatially downscaled sun-induced fluorescence global product for enhanced monitoring of vegetation productivity. *Earth Syst. Sci. Data* 12, 1101–1116. <https://doi.org/10.5194/essd-12-1101-2020>.
- Ferrenberg, S., Tucker, C.L., Reed, S.C., 2017. Biological soil crusts: diminutive communities of potential global importance. *Front. Ecol. Environ.* 15 (3), 160–167.
- Flanagan, L.B., Sharp, E.J., Gamon, J.A., 2015. Application of the photosynthetic light-use efficiency model in a northern Great Plains grassland. *Remote Sens. Environ.* 168, 239–251. <https://doi.org/10.1016/j.rse.2015.07.013>.
- Gentine, P., Alemohammad, S.H., 2018. Reconstructed solar-induced fluorescence: a machine learning vegetation product based on MODIS surface reflectance to reproduce GOME-2 solar-induced fluorescence. *Geophys. Res. Lett.* 45, 3136–3146. <https://doi.org/10.1002/2017GL076294>.
- Gholami Baghi, N., Oldeland, J., 2019. Do soil-adjusted or standard vegetation indices better predict above ground biomass of semi-arid, saline rangelands in North-East Iran? *Int. J. Remote Sens.* 40, 8223–8235. <https://doi.org/10.1080/01431161.2019.1606958>.
- Gitelson, A.A., Peng, Y., Huemmrich, K.F., 2014. Relationship between fraction of radiation absorbed by photosynthesizing maize and soybean canopies and NDVI from remotely sensed data taken at close range and from MODIS 250m resolution data. *Remote Sens. Environ.* 147, 108–120. <https://doi.org/10.1016/j.rse.2014.02.014>.
- Guanter, L., Alonso, L., Gómez-Chova, L., Amorós-López, J., Vila, J., Moreno, J., 2007. Estimation of solar-induced vegetation fluorescence from space measurements. *Geophys. Res. Lett.* 34, 1–5. <https://doi.org/10.1029/2007GL029289>.
- Guanter, L., Zhang, Y., Jung, M., Joiner, J., Voigt, M., Berry, J.A., Frankenberg, C., Huete, A.R., Zarco-Tejada, P., Lee, J.-E., Moran, M.S., Ponce-Campos, G., Beer, C., Camps-Valls, G., Buchmann, N., Gianelle, D., Klumpp, K., Cescatti, A., Baker, J.M., Griffis, T.J., 2014. Global and time-resolved monitoring of crop photosynthesis with chlorophyll fluorescence. *Proc. Natl. Acad. Sci.* 111, E1327–E1333. <https://doi.org/10.1073/pnas.1320008111>.
- Guanter, L., Aben, I., Tol, P., Krijger, J.M., Hollstein, A., Köhler, P., Damm, A., Joiner, J., Frankenberg, C., Landgraf, J., 2015. Potential of the TROPospheric Monitoring Instrument (TROPOMI) onboard the Sentinel-5 precursor for the monitoring of terrestrial chlorophyll fluorescence. *Atmos. Meas. Tech.* 8, 1337–1352. <https://doi.org/10.5194/amt-8-1337-2015>.
- Hao, D., Zeng, Y., Qiu, H., Biriukova, K., Celesti, M., Migliavacca, M., Rossini, M., Asrar, G.R., Chen, M., 2020. Practical approaches for normalizing directional solar-induced fluorescence to a standard viewing geometry. *Remote Sens. Environ.* 112171 <https://doi.org/10.1016/j.rse.2020.112171>.
- Hao, D., Asrar, G.R., Zeng, Y., Yang, X., Li, X., Xiao, J., Guan, K., Wen, J., Xiao, Q., Berry, J.A., Chen, M., 2021. Potential of hotspot solar-induced chlorophyll fluorescence for better tracking terrestrial photosynthesis. *Glob. Chang. Biol.* 27, 2144–2158. <https://doi.org/10.1111/gcb.15554>.
- He, L., Magney, T., Dutta, D., Yin, Y., Köhler, P., Grossmann, K., Stutz, J., Dold, C., Hatfield, J., Guan, K., Peng, B., Frankenberg, C., 2020. From the ground to space: using solar-induced chlorophyll fluorescence to estimate crop productivity. *Geophys. Res. Lett.* 47 <https://doi.org/10.1029/2020GL07474>.
- Huang, J., Yu, H., Guan, X., Wang, G., Guo, R., 2016. Accelerated dryland expansion under climate change. *Nat. Clim. Chang.* 6, 166–171. <https://doi.org/10.1038/nclimate2837>.
- Huang, J., Yu, H., Dai, A., Wei, Y., Kang, L., 2017. Drylands face potential threat under 2 °C global warming target. *Nat. Clim. Chang.* 7, 417–422. <https://doi.org/10.1038/nclimate3275>.
- Huete, A.R., 1988. A soil-adjusted vegetation index (SAVI). *Remote Sens. Environ.* 25, 295–309.
- Joiner, J., Yoshida, Y., Vasilkov, A.P., Schaefer, K., Jung, M., Guanter, L., Zhang, Y., Garrity, S., Middleton, E.M., Huemmrich, K.F., Gu, L., Belletti Marchesini, L., 2014. The seasonal cycle of satellite chlorophyll fluorescence observations and its relationship to vegetation phenology and ecosystem atmosphere carbon exchange. *Remote Sens. Environ.* 152, 375–391. <https://doi.org/10.1016/j.rse.2014.06.022>.
- Jones, M.O., Allred, B.W., Naugle, D.E., Maestas, J.D., Donnelly, P., Metz, L.J., Karl, J., Smith, R., Bestelmeyer, B., Boyd, C., Kerby, J.D., McIver, J.D., 2018. Innovation in rangeland monitoring: annual, 30 m, plant functional type percent cover maps for U. S. rangelands, 1984–2017. *Ecosphere* 9. <https://doi.org/10.1002/ecs2.2430>.
- Knowles, J.F., Scott, R.L., Biederman, J.A., Blanken, P.D., Burns, S.P., Dore, S., Kolb, T.E., Litvak, M.E., Barron-Gafford, G.A., 2020. Montane forest productivity across a semi-arid climatic gradient. *Glob. Chang. Biol.* 26 (12), 6945–6958. <https://doi.org/10.1111/gcb.15335>.
- Köhler, P., Frankenberg, C., Magney, T.S., Guanter, L., Joiner, J., Landgraf, J., 2018. Global retrievals of solar induced chlorophyll fluorescence with TROPOMI: first results and inter-sensor comparison to OCO-2. *Geophys. Res. Lett.* 456–463 <https://doi.org/10.1029/2018GL079031>.
- Köhler, P., Fischer, W.W., Rossman, G.R., Grotzinger, J.P., Doughty, R., Wang, Y., Yin, Y., Frankenberg, C., 2021. Mineral luminescence observed from space. *Geophys. Res. Lett.* 48, 1–10. <https://doi.org/10.1029/2021GL095227>.
- Lasslop, G., Reichstein, M., Papale, D., Richardson, A.D., Arneeth, A., Barr, A., Wohlfahrt, G., 2010. Separation of net ecosystem exchange into assimilation and respiration using a light response curve approach: critical issues and global evaluation. *Glob. Chang. Biol.* 16, 187–208. <https://doi.org/10.1111/j.1365-2486.2009.02041.x>.
- Law, B.E., Waring, R.H., 2011. In: Law, Beverly E., Waring, Richard H. (Eds.), *Remote Sensing of Leaf Area Index and Radiation Intercepted by Understory Vegetation*

- Author (s), 4. Ecological Society of America Stable, pp. 272–279. URL : <http://www.jstor.org/stable/1941933> . Remote Sensing of Lea. America (NY).
- Liu, Y., Hill, M.J., Zhang, X., Wang, Z., Richardson, A.D., Hufkens, K., Filippa, G., Baldocchi, D.D., Ma, S., Verfaillie, J., Schaaf, C.B., 2017. Using data from Landsat, MODIS, VIIRS and PhenoCams to monitor the phenology of California oak/grass savanna and open grassland across spatial scales. *Agric. For. Meteorol.* 237–238, 311–325. <https://doi.org/10.1016/j.agrformet.2017.02.026>.
- Ma, S., Baldocchi, D.D., Xu, L., Hehn, T., 2007. Inter-annual variability in carbon dioxide exchange of an oak/grass savanna and open grassland in California. *Agric. For. Meteorol.* 147 (3–4), 157–171.
- Ma, X., Huete, A., Moore, C.E., Cleverly, J., Hutley, L.B., Beringer, J., Leng, S., Xie, Z., Yu, Q., Eamus, D., 2020. Spatiotemporal partitioning of savanna plant functional type productivity along NATT. *Remote Sens. Environ.* 246, 111855 <https://doi.org/10.1016/j.rse.2020.111855>.
- Magney, T.S., Bowling, D.R., Logan, B., Grossmann, K., Stutz, J., Blanken, P., 2019. Mechanistic evidence for tracking the seasonality of photosynthesis with solar-induced fluorescence. *Proc. Natl. Acad. Sci.* <https://doi.org/10.1073/pnas.19002781166>, 201900278.
- Mengistu, A.G., Mengistu Tsidu, G., Koren, G., Kooreman, M.L., Boersma, K.F., Peters, W., 2020. Sun-induced fluorescence and near infrared reflectance of vegetation track the seasonal dynamics of gross primary production over Africa. *Biogeosciences*. <https://doi.org/10.5194/bg-2020-242>. In Press.
- Migliavacca, M., Perez-Priego, O., Rossini, M., El-Madany, T.S., Moreno, G., van der Tol, C., Rascher, U., Berninger, A., Bessenbacher, V., Burkart, A., Carrara, A., Fava, F., Guan, J.H., Hammer, T.W., Henkel, K., Juarez-Alcalde, E., Julitta, T., Kolle, O., Martín, M.P., Musavi, T., Pacheco-Labrador, J., Pérez-Burguño, A., Wutzler, T., Zaehle, S., Reichstein, M., 2017. Plant functional traits and canopy structure control the relationship between photosynthetic CO₂ uptake and far-red sun-induced fluorescence in a Mediterranean grassland under different nutrient availability. *New Phytol.* 214, 1078–1091. <https://doi.org/10.1111/nph.14437>.
- Nestola, E., Calafapietra, C., Emmerton, C.A., Wong, C.Y.S., Thayer, D.R., Gamon, J.A., 2016. Monitoring grassland seasonal dynamics, by integrating MODIS NDVI, proximal optical sampling, and eddy covariance measurements. *Remote Sens.* 8 <https://doi.org/10.3390/rs8030260>.
- Peng, Y., Nguy-Robertson, A., Arkebauer, T., Gitelson, A.A., 2017. Assessment of canopy chlorophyll content retrieval in maize and soybean: implications of hysteresis on the development of generic algorithms. *Remote Sens.* 9 <https://doi.org/10.3390/rs9030226>.
- Poulter, B., Frank, D., Ciais, P., Myneni, R.B., Andela, N., Bi, J., Broquet, G., Canadell, J.G., Chevallier, F., Liu, Y.Y., Running, S.W., Stith, S., Van Der Werf, G.R., 2014. Contribution of semi-arid ecosystems to interannual variability of the global carbon cycle. *Nature* 509, 600–603. <https://doi.org/10.1038/nature13376>.
- Qiu, B., Chen, J.M., Ju, W., Zhang, Q., Zhang, Y., 2019. Simulating emission and scattering of solar-induced chlorophyll fluorescence at far-red band in global vegetation with different canopy structures. *Remote Sens. Environ.* 233, 111373 <https://doi.org/10.1016/j.rse.2019.111373>.
- Reichstein, M., Falge, E., Baldocchi, D., et al., 2005. On the separation of net ecosystem exchange into assimilation and ecosystem respiration: review and improved algorithm. *Glob. Chang. Biol.* 11, 1424–1439.
- Reynolds, J.F., Stafford Smith, D.M., Lambin, E.F., Turner, B.L., Mortimore, M., Batterbury, S.P.J., Downing, T.E., Dowlatabadi, H., Fernández, R.J., Herrick, J.E., Huber-Sannwald, E., Jiang, H., Leemans, R., Lynam, T., Maestre, F.T., Ayarza, M., Walker, B., 2007. Ecology: global desertification: building a science for dryland development. *Science* 80 (316), 847–851. <https://doi.org/10.1126/science.1131634>.
- Richardson, A.J., Everitt, J.H., 1992. Using spectral vegetation indices to estimate rangeland productivity. *Geocart. Int.* 7 (1), 63–69.
- Robinson, N.P., Allred, B.W., Smith, W.K., Jones, M.O., Moreno, A., Erickson, T.A., Naugle, D.E., Running, S.W., 2018. Landsat 30 m and MODIS 250 m derived terrestrial primary production for the conterminous United States. In: *Remote Sensing in Ecology and Conservation*. <https://doi.org/10.1002/rse2.74>.
- Romero, J.M., Cordon, G.B., Lagorio, M.G., 2018. Modeling re-absorption of fluorescence from the leaf to the canopy level. *Remote Sens. Environ.* 204 (0), 138–146.
- Scott, R.L., Jenerette, G.D., Potts, D.L., Huxman, T.E., 2009. Effects of seasonal drought on net carbon dioxide exchange from a woody-plant-encroached semiarid grassland. *J. Geophys. Res. Biogeosci.* 114 (G4).
- Sellers, P.J., Berry, J.A., Collatz, G.J., Field, C.B., Hall, E.G., 1992. Canopy reflectance, photosynthesis, and transpiration. III. Areal analysis using improved leaf models and a new canopy integration scheme. *Remote Sens. Environ.* 42, 187–216.
- Seyednasrollah, B., Bowling, D.R., Cheng, R., Logan, B.A., Magney, T.S., Frankenberg, C., Yang, J.C., Young, A.M., Hufkens, K., Arain, M.A., Black, T.A., Blanken, P.D., Bracho, R., Jassal, R., Hollinger, D.Y., Law, B.E., Nesic, Z., Richardson, A.D., 2020. Seasonal variation in the canopy color of temperate evergreen conifer forests. *New Phytol.* <https://doi.org/10.1111/nph.17046>.
- Smith, W.K., Reed, S.C., Ballantyne, A.P., Cleveland, C.C., Anderegg, W.R.L., Wieder, W.R., Running, S.W., 2016. Large divergence of satellite and earth system model estimates of global terrestrial CO₂ fertilization. *Nat. Clim. Chang.* 6, 306–310.
- Smith, W.K., Biederman, J.A., Scott, R.L., Moore, D.J.P., He, M., Kimball, J.S., Yan, D., Hudson, A., Barnes, M.L., MacBean, N., Fox, A.M., Litvak, M.E., 2018. Chlorophyll fluorescence better captures seasonal and interannual gross primary productivity dynamics across dryland ecosystems of southwestern North America. *Geophys. Res. Lett.* 45, 748–757. <https://doi.org/10.1002/2017GL075922>.
- Smith, W.K., Dannenberg, M.P., Yan, D., Herrmann, S., Barnes, M.L., Barron-Gafford, G.A., Biederman, J.A., Ferrenberg, S., Fox, A.M., Hudson, A., Knowles, J.F., MacBean, N., Moore, D.J.P., Nagler, P.L., Reed, S.C., Rutherford, W.A., Scott, R.L., Wang, X., Yang, J., 2019. Remote sensing of dryland ecosystem structure and function: progress, challenges, and opportunities. *Remote Sens. Environ.* 233, 111401 <https://doi.org/10.1016/j.rse.2019.111401>.
- Sun, Y., Frankenberg, C., Wood, J.D., Schimel, D.S., Jung, M., Guanter, L., Drewry, D.T., Verma, M., Porcar-Castell, A., Griffiths, T.J., Gu, L., Magney, T.S., Köhler, P., Evans, B., Yuen, K., 2017. OCO-2 advances photosynthesis observation from space via solar-induced chlorophyll fluorescence. *Science* 80, 358. <https://doi.org/10.1126/science.aam5747>.
- Templeton, R.C., Vivoni, E.R., Méndez-Barroso, L.A., Pierini, N.A., Anderson, C.A., Rango, A., Laliberte, A.S., Scott, R.L., 2014. High-resolution characterization of a semiarid watershed: implications on evapotranspiration estimates. *J. Hydrol.* 509, 306–319.
- Tucker, C.J., 1979. Red and photographic infrared linear combinations for monitoring vegetation. *Remote Sens. Environ.* 8, 127–150.
- Turner, A.J., Köhler, P., Magney, T.S., Frankenberg, C., Fung, I., Cohen, R.C., 2020. A double peak in the seasonality of California's photosynthesis as observed from space. *Biogeosciences* 1–27. <https://doi.org/10.5194/bg-2019-387>.
- Turner, A.J., Köhler, P., Magney, T.S., Frankenberg, C., Fung, I., Cohen, R.C., 2021. Extreme events driving year-to-year differences in gross primary productivity across the US. *Biogeosci. Discuss.* <https://doi.org/10.5194/bg-2021-49> [preprint].
- Verma, M., Friedl, M.A., Richardson, A.D., Kiely, G., Cescatti, A., Law, B.E., Wohlfahrt, G., Gielen, B., Rouspard, O., Moors, E.J., Toscano, P., Vaccari, F.P., Gianelle, D., Bohrer, G., Varlagin, A., Buchmann, N., Van Gorsel, E., Montagnani, L., Propastin, P., 2014. Remote sensing of annual terrestrial gross primary productivity from MODIS: an assessment using the FLUXNET la Thuile data set. *Biogeosciences* 11, 2185–2200. <https://doi.org/10.5194/bg-11-2185-2014>.
- Walther, S., Voigt, M., Thum, T., Gonsamo, A., Zhang, Y., Köhler, P., Jung, M., Varlagin, A., Guanter, L., 2016. Satellite chlorophyll fluorescence measurements reveal large-scale decoupling of photosynthesis and greenness dynamics in boreal evergreen forests. *Glob. Chang. Biol.* 22, 2979–2996. <https://doi.org/10.1111/gcb.13200>.
- Wang, C., Beringer, J., Hutley, L.B., Cleverly, J., Li, J., Liu, Q., Sun, Y., 2019. Phenology dynamics of dryland ecosystems along the north Australian tropical transect revealed by satellite solar-induced chlorophyll fluorescence. *Geophys. Res. Lett.* 46, 5294–5302. <https://doi.org/10.1029/2019GL082716>.
- Wang, R., Gamon, J.A., Emmerton, C.A., Springer, K.R., Yu, R., Hminina, G., 2020a. Detecting intra- and inter-annual variability in gross primary productivity of a North American grassland using MODIS MAIAC data. *Agric. For. Meteorol.* 281, 107859 <https://doi.org/10.1016/j.agrformet.2019.107859>.
- Wang, X., Dannenberg, M.P., Yan, D., Jones, M.O., Kimball, J.S., Moore, D.J.P., van Leeuwen, W.J.D., Didan, K., Smith, W.K., 2020b. Globally consistent patterns of asynchrony in vegetation phenology derived from optical, microwave, and fluorescence satellite data. *J. Geophys. Res. Biogeosci.* 125 <https://doi.org/10.1029/2020JG005732>.
- Wu, C., Gonsamo, A., Gough, C.M., Chen, J.M., Xu, S., 2014. Modeling growing season phenology in North American forests using seasonal mean vegetation indices from MODIS. *Remote Sens. Environ.* 147, 79–88. <https://doi.org/10.1016/j.rse.2014.03.001>.
- Xu, L.K., Baldocchi, D.D., 2003. Seasonal trends in photosynthetic parameters and stomatal conductance of blue oak (*Quercus douglasii*) under prolonged summer drought and high temperature. *Tree Physiol.* 23 (13), 865–877.
- Yan, D., Scott, R.L., Moore, D.J.P., Biederman, J.A., Smith, W.K., 2019. Understanding the relationship between vegetation greenness and productivity across dryland ecosystems through the integration of PhenoCam, satellite, and eddy covariance data. *Remote Sens. Environ.* 223, 50–62. <https://doi.org/10.1016/j.rse.2018.12.029>.
- Yao, J., Liu, H., Huang, J., Gao, Z., Wang, G., Li, D., Yu, H., Chen, X., 2020. Accelerated dryland expansion regulates future variability in dryland gross primary production. *Nat. Commun.* 11, 1–10. <https://doi.org/10.1038/s41467-020-15515-2>.
- Zhao, B., Duan, A., Ata-Ul-Karim, S.T., Liu, Zhandong, Chen, Z., Gong, Z., Zhang, J., Xiao, J., Liu, Zugui, Qin, A., Ning, D., 2018. Exploring new spectral bands and vegetation indices for estimating nitrogen nutrition index of summer maize. *Eur. J. Agron.* 93, 113–125. <https://doi.org/10.1016/j.eja.2017.12.006>.
- Zuromski, L.M., Bowling, D.R., Köhler, P., Frankenberg, C., Goulden, M.L., Blanken, P.D., Lin, J.C., 2018. Solar-induced fluorescence detects interannual variation in gross primary production of coniferous forests in the western United States. *Geophys. Res. Lett.* 45, 7184–7193. <https://doi.org/10.1029/2018GL077906>.